Multi-material freeform 3D printing of flexible piezoelectric composite sensors using a supporting fluid

Rui Tao, Floriane Granier, and Daniel Therriault[*]

Laboratory for Multiscale Mechanics (LM²), Department of Mechanical Engineering, Research Center for High Performance Polymer and Composite Systems (CREPEC), Polytechnique Montreal, Montreal, QC, H3T 1J4, Canada

* Corresponding author: daniel.therriault@polymtl.ca

Abstract

Three-dimensional (3D) printed flexible piezoelectric devices featuring conformal or freeform geometries show great potential for being fabricated into wireless sensors and energy harvesters with tailorable mechanical stiffness and piezoelectric response. In our work, supporting fluid-assisted multi-material extrusion-based 3D printing technology has been successfully utilized to fabricate flexible conformal or freeform piezoelectric composite sensors with integrated electrodes. The printing technique relies on the extrusion of two paste-like materials: piezoelectric and conductive composite inks. A comprehensive characterization of the inks (i.e., piezoelectric or conductive behaviors, rheological and mechanical properties) and the rheological behavior of the supporting fluid are performed. Polydimethylsiloxane (PDMS)/30vol% lead zirconate titanate (PZT), PDMS/25vol% silver (Ag) and mineral oil/6% (w/v) fumed silica are the formulations for piezoelectric ink, conductive ink and supporting fluid, respectively. Three types of piezoelectric composite demonstrators which are a multi-layer planar film, a conformal non-planar hemisphere and a 3D structure composed of six spirals printed vertically between two hexagon layers (freeform spiral-hexagon), are fabricated and tested under tension or compression tests. The piezoelectric

performance is consistent with the applied stress in all the tests. For example, the freeform spiral-hexagon piezoelectric sensor has a peak-to-peak voltage output of 86.39 $\pm$ 1.145 mV when it is subjected to a cyclic compression force at 8 Hz for more than 800 cycles. The dimensional accuracy measurements using an optical microscope and the microstructure images taken using a scanning electron microscope (SEM) show that the fabricated 3D structures have good shape fidelity (with a maximum relative error of ~3.5%) when compared to the designed models. Our fabrication approach opens a new way to fabricate conformal and freeform piezoelectric structures with integrated electrodes from flexible composites for sensing and energy harvesting applications.

Keywords

Multi-material additive manufacturing; Freeform 3D printing; Conformal 3D printing; Piezoelectric; Composite; Sensors

1   Introduction

Recent interests in wireless wearable piezoelectric sensors, flexible energy harvesters, and smart artificial skins have led to scores of investigations on stretchable piezoelectric materials [1–7]. These devices seek for new fabrication schemes that enable the fabrication of conformal and freeform complex geometries [8–11]. Conformal geometries feature uneven or curved surfaces [12]. Freeform geometries are more complex than conformal 3D geometries, which represent freedom design structures [13]. The freeform geometries have the advantages of being more compact (i.e., lightweight) and having greater design feasibility.

Additive manufacturing, also referred as three-dimensional (3D) printing, is a family of several processes that enables the fabrication of a 3D shape usually in a layer-by-layer approach. Traditionally, extrusion-based 3D printing methods such as direct-ink writing (DIW) technique

2

are used to print freeform structures. As first, the inks should possess a shear-thinning behavior, which can benefit the flowability through the dispensing needle [14,15]. After the ink was extruded out of the needle, the shear stress is relieved and the ink viscosity increases again, which helps to retain its shape. Also, the functional ink materials must exhibit rapid solidification properties to retain the shape as extruded. There are usually two ways to enable rapid solidification: one way is to use fast-evaporation solvents [16] that are usually toxic; another way is to use ultraviolet (UV)-assisted DIW 3D printing technique, but this significantly limits the choice of printable materials [17,18]. To address these challenges, embedded 3D printing (e-3DP) [19–23] or DIW 3D printing in the supporting fluid [24] techniques have been developed to fabricate soft tissues or strain sensors for biomedical applications. The supporting fluid behaves as a Herschel-Bulkley fluid. The deposited filament is physically entrapped in the space between the crosslinked microgels, which temporarily flow under the stress generated by a moving dispensing needle and then rapidly recover to a jammed solid state to support the deposited filaments [25,26]. In addition, optically transparent, non-toxic and easy to clean properties are also the requirements for the supporting fluids. A variety of supporting fluid materials such as mineral oil/fumed silica [27], deionized water (DW)/dry Laponite [28,29], DW/Carbopol [30–33], DW/pluronic F-127 [34,35], DW/low acyl Gellan Gum [36,37], DW/alginate [38,39], Ultrez 30/Carbopol [40], PF-CaCl$_2$/Laponite [13,41], and DW/poloxamer/poly(ethylene glycol) [42] have been investigated.

An issue related to the manufacturing of piezoelectric devices is that an extra step is usually required to add electrodes on the piezoelectric elements for collecting the generated charges. The commonly used techniques to create the electrodes are painting [43], screen printing [44], sputtering [45] or attaching conductive tape or fabrics [46,47]. Several researchers have fabricated piezoelectric elements and electrodes in a single manufacturing process. Lu *et al.* developed

3

thermal-mechanically drawn piezoelectric fibers consisting of alternating layers of piezoelectric electrospun nanocomposites (polyvinylidene fluoride enhanced with barium titanate, PZT or carbon nanotubes) and commercially available conductive composites (i.e., carbon black filled polyethylene) [48,49]. Bodkhe *et al.* co-extruded piezoelectric filament with integrated electrodes using DIW technique [50]. Also, several researchers used a multi-material 3D printing technology [51–53] to co-fabricate electrodes with 3D piezoelectric structure in a single manufacturing process [54]. However, the fabricated structures are limited to one-dimensional fiber, two dimensional film or simple 3D scaffold shapes.

This work presents a fabrication approach based on multi-material DIW 3D printing in a supporting fluid bath to fabricate multi-layer, conformal and freeform flexible piezoelectric sensors with integrated electrodes in a single manufacturing process. Various concentrations of fumed silica nanoparticles were added into the mineral oil to find the best supporting behavior of the mineral oil/fumed silica supporting fluid with the proper yield stress. We also developed flexible piezoelectric polydimethylsiloxane (PDMS)/PZT and conductive PDMS/Ag composite materials as printing inks. The piezoelectric and conductive, rheological, and mechanical properties of the inks were investigated. The dimensional accuracy and piezoelectric performance of the three types of multi-material piezoelectric composite demonstrators prove that the developed composite materials and manufacturing technique could be further employed for the production of various freeform and conformal piezoelectric sensing and energy harvesting applications.

2 Experimental section

2.1 Materials

Inks: A mixture of two different types of PDMS was used as the matrix for both piezoelectric and conductive composite inks. The low viscosity PDMS (SYLGARD™ 184) and high viscosity PDMS (DOWSIL™ SE 1700) were purchased from DOW Chemical (USA). The weight ratio of the high to low viscosity PDMS is 7:3, as recommended by the relevant works [55,56] and the base to curing agent is 10:1, as recommended by the supplier. The addition of low viscosity PDMS acted on the dilution of high viscosity PDMS for desired rheological properties. The PZT powder (APC 850: ~500 nm, spherical particles) was purchased from APC International, Ltd (USA) as the filler for piezoelectric composite ink. The silver flake powder (47MR-10F: purity = 99.95%, 2–5 μm) was purchased from Inframat Advanced Materials (USA) as the filler for the conductive composite ink.

Supporting Fluid: The fumed silica powder (AEROSIL® R805: 200 m^2/g) was purchased from Evonik Industries (USA) and the mineral oil (CAS: 8042-47-5) from VWR (Canada).

2.2 Manufacturing process

2.2.1 Inks and supporting fluid preparation process

Piezoelectric ink: 30 vol% PZT powder was added into the PDMS system and blended in a mixer (DAC 515-200 SE, FlackTeck SpeedMixer®) at 2750 rpm for 1 min.

Conductive ink: 25 vol% Ag flakes was added into the mixture of PDMS and blended in the mixer at 2750 rpm for 1 min. Then the two types of inks were loaded into two syringe barrels (3 mL, Nordson EFD), respectively.

5

Supporting fluid: 6% (w/v) fumed silica was blended with mineral oil in a 60 ml mixer container at 2750 rpm for 1 min. Then, the supporting fluid rested for 10 min and was remixed for 1 min to remove the bubbles (Fig. 1a).

2.2.2 *Multi-material DIW 3D printing of piezoelectric composite structures with integrated electrodes*

Multi-material 3D printing process was carried out using a three-axis motion-controlled gantry system (Aerotech, USA) equipped with two independent DIW printing heads: one DIW head was assigned for the piezoelectric ink and the other DIW head was assigned for the conductive ink (Fig. 1b). A custom-made pneumatic-driven controller (Mëkanic, Canada) was used to apply the pressure on the piston of dispensing apparatus (EFD 7×, Nordson) to push the ink inside the syringe out of the nozzle along the print paths. In the case of multi-layer planar films and conformal non-planar hemispheres, print paths were initially generated with Simplify3D slicing software and then translated to the Aerobasic language (i.e., the language of Aerotech) using a robotic simulation software, RoboDK 4.2.4 (RoboDK Inc.). In the case of the freeform spiral-hexagon structure, the print paths were generated using a custom-made MATLAB program and then translated to Aerobasic language using RoboDK. The printing speed was 5 mm/s. The applied pressure was 210 kPa for the conductive ink and 280 kPa for the piezoelectric ink, respectively. The dispensing needle of the nozzle had a 38 mm-long stainless steel tip (Nordson EFD) and an inner diameter of 0.6 mm. The fairly long nozzle was selected to ensure that the nozzle can reach the bottom section of the supporting fluid. The layer height was 0.5 mm.

6

2.2.3   *Post-curing process*

The fabricated piezoelectric structures were cured in an oven at 80°C for 24 h (Fig. 1c). We selected 80°C because the boiling point of the mineral oil is 100°C. Then the cured structures were taken out of the supporting fluid and washed with soap and water to remove the residue of mineral oil and fumed silica and dried at ambient temperature. The supporting fluid can be reused multiple times.

2.2.4   *Poling process*

To orient the dipole moments of the fabricated piezoelectric composite structures in the desired direction, a contact poling setup was built (Fig. 1d). The setup consists of three parts: a custom-made poling station, a high voltage power supply (ES60kV negative, 10 Watt, Gamma High Voltage Research, Inc.) and a hot plate (Thermo Scientific™ SuperNuova+™, Fisher Scientific). In the poling station, an aluminum plate was grounded, and a negative high voltage cable from the high voltage power supply was connected to a copper rod (~3 mm in diameter) as the poling head. An aluminum plate ($20 \times 20 \times 2$ mm^3) was inserted between the copper rod of the poling head and top surface of the element to achieve a good distribution of electric field. During the poling process, we put the piezoelectric structure between the poling head and bottom aluminum plate, and polarized it under an electric field of 5 kV/mm at 80°C for 60 min. After the poling process, the piezoelectric structure was cooled down to room temperature before removing the electric field to reduce the misalignment of dipole moments. The piezoelectric structure was finally washed with soap and water to remove the residue of silicone oil and dried at ambient temperature.
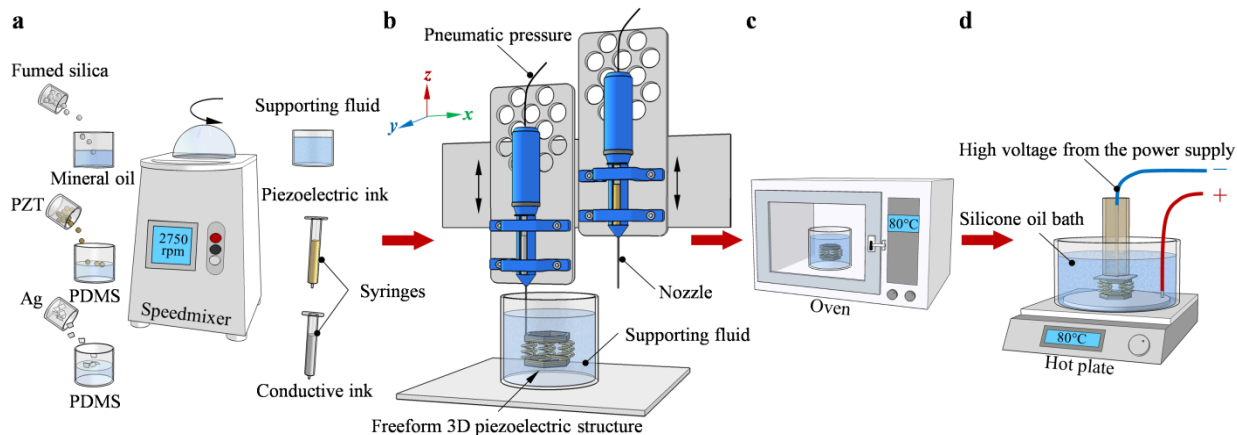
7

Fig. 1. Fabrication of multi-material freeform 3D printed flexible piezoelectric composite sensors with integrated electrodes in the mineral oil/fumed silica supporting fluid: (a) Inks and supporting fluid preparation process using a mixer (piezoelectric composite ink: PDMS/30vol%PZT; conductive composite ink: PDMS/25vol%Ag; supporting fluid: mineral oil/6%(w/v) fumed silica). (b) Multi-material freeform 3D printing process in the supporting fluid (freeform spiral-hexagon is shown). (c) Curing process in an oven. (d) Poling process using a custom-made poling station.

2.3 Scanning electron microscopy (SEM) and optical characterization

The SEM observations (TM3030, Hitachi, USA) were used to investigate the microstructures of the following samples: (1) the bonding section of the printed piezoelectric and electrode layers cut from the multi-layer planar film; (2) printed layers, and (3) printed filaments cut from the conformal non-planar hemisphere structure (PDMS/30vol%PZT and PDMS/25vol%Ag composites); (4) a PDMS/30vol%PZT composite spiral cut from the freeform spiral-hexagon. A razor blade was used to cut all these samples. Samples were then sputtered with a 10 nm layer of chrome before the imaging analysis. The imaging analyses were performed at a 5 kV voltage supply. Filler dispersion was analysed based on the cross-sectional view of the sample (3) which were fractured manually in the liquid nitrogen. The dimensions of the three types of piezoelectric composite structures were measured using an optical microscope (BX-61, Olympus) and software ImageJ (version 1.8.0_172).

8

2.4 Piezoelectric coefficient characterization

A d_{33} meter (YE2730, Sinocera Piezotronics, Inc.) was used to characterize the piezoelectric coefficient - d_{33} of the PDMS/PZT composite films ($50 \times 10 \times 0.5$ mm^3) made of different PZT volume fractions (10, 20, 30 and 40 vol%). Five specimens of each type were tested approximately one day after the poling process to measure a stabilized value.

2.5 Piezoelectric test on the multi-material 3D printed piezoelectric composite structures

The piezoelectric performances of the three types of piezoelectric composite structures with integrated electrodes were evaluated through the following three tests: (1) stretching-relaxation test (axial strain = 10%, 3 cycles) of the multi-layer planar film ($50 \times 20 \times 1.5$ mm^3) was carried out using an MTS Insight machine at a crosshead speed of 1 mm/s. The gage length is 20 mm; (2) finger tapping test was conducted on the conformal non-planar hemisphere by three gentle finger taps; (3) cyclic compression tests (displacement = 2 mm, f = 8 Hz, 800 cycles) of the freeform spiral-hexagon using a shaker (2060E, Mode Shop Inc.).

The open-circuit piezoelectric voltages were collected using a charge amplifier (Piezo Lab Amplifier, MEAS Specialties) in a voltage mode. The voltage data was acquired with an NI-9239 data acquisition system attached to a USB carrier NI-9162 (National Instruments) and recorded using a custom LabVIEW interface.

2.6 Conductivity measurement on the conductive composite films

The electrical resistance (R) was measured using a four-point resistance measuring card (PCI-4070 card, National 312 Instruments). The R of the printed PDMS/Ag composite films ($50 \times 10 \times 0.5$ mm^3) with different Ag volume fractions (20, 25 and 30 vol%) were measured. Five specimens of each volume fraction were tested.

2.7 Rheological characterization

Shear viscosities of PDMS/PZT, PDMS/Ag composite inks and mineral oil/fumed silica supporting fluid with different filler concentrations were measured using a controlled stress rheometer (MCR 502, Anton Paar) equipped with parallel plates at shear rates between 0.001 to 100 s^{-1} at ambient temperature. Also, the process-related viscosity measurements on the PDMS/PZT and PDMS/Ag inks were conducted by capillary flow analysis following the procedure described in [57]. Different concentrations of PDMS/PZT (10, 20 and 30 vol%) and PDMS/Ag inks (25 and 30 vol%) were extruded on glass substrates under five different applied pressures at a print head motion velocity of 0.5 mm/s. The extruded filaments (~60 mm long) were weighed using a high-precision balance (GH-202, A&D Engineering Inc.). Their weight was used to obtain the volumetric flow rates for calculating the process-related apparent viscosity of the various inks. Three specimens of each type were tested.

2.8 Mechanical characterization

The tensile stiffness and elongation at break (%) characterization of the one-layer piezoelectric PDMS/PZT composite rectangular films (50 × 10 × 0.5 mm^3) with three PZT volume fractions (10, 20 and 30 vol%), and the one-layer conductive PDMS/Ag composite rectangular films (50 × 10 × 0.5 mm^3) with two Ag volume fractions (25 and 30 vol%) were carried out using an MTS Insight electromechanical testing system (820-050-EL) with a 100 N load cell at a crosshead speed of 50 mm/min. The gauge length was 25 mm. The test was carried out based on ASTM Standard D882 - 12. Five specimens of each type were tested.

10

3 Results and discussion

Fig. 2 presents the supporting performance of the supporting fluid with different compositions, the mechanism and the required rheological behavior. Fig. 2a schematically illustrates a single filament deposited in the supporting fluid with different fumed silica concentrations, the images are shown in Fig. S1. The deposited filament is discontinuous and dragged by the dispensing needle in the 5% (w/v) supporting fluid (Fig. 2aI). When the concentration of fumed silica is too high, i.e., above 7% (w/v), the crevasse can be seen along the movement of the dispensing needle (Fig. 2aIII). The crevasse adversely affects the following support performance of the supporting fluid. In the 6% (w/v) supporting fluid, the deposited filament is well supported without the introduction of any crevasse (Fig. 2aII).[25]

The mechanism of the supporting performance of mineral oil/fumed silica is illustrated in Fig. 2b.[27] When the dispensing needle moves in the mineral oil/6%(w/v) fumed silica supporting fluid, the shear stress induced by the dispensing needle is higher than the yield stress of the supporting fluid. Thus, the fumed silica aggregates are disrupted and flow like fluid to fill out the crevasse induced by the needle movement. Conversely, the scattered fumed silica aggregates recover to the stable 3D network when the dispensing needle leaves. Therefore, the fumed silica aggregates are stable like solid to support the deposited filaments.

The yield stress is the transition threshold between solid and fluid states of the mineral oil/fumed silica supporting fluid. The supporting fluid having a yield stress behaves like solid when the applied stress is lower than the yield stress, while it flows like fluid when the applied stress is higher than the yield stress.[27,29] To obtain the yield stress, the mineral oil/fumed silica nanoparticle suspensions with different compositions were tested in a rheometer in a steady sweep mode at different shear rates and the corresponding shear stresses were recorded. As illustrated in Fig. 2c, we observed that for suspensions with different nanoparticle concentrations, shear stress

increases with the increase of shear rate. The yield stress also increases with the addition of the fumed silica concentration. The yield stresses of the fumed silica nanoparticle suspensions are calculated by fitting the shear stress τ and shear rate $\dot{\gamma}$ data in the Herschel-Bulkley model [58]:

$$\tau = \tau_0 + k\dot{\gamma}^n \tag{1}$$

where τ_0 is the yield stress (Pa), n is the flow index, and k is the consistency index (Pa·s^n). The respective fitted Herschel-Bulkley parameters τ_0, n and k are listed in Table 1. The model shows good agreement with the rheometry data in both low and high $\dot{\gamma}$ regions, confirming the choice of the Herschel-Bulkley model to calculate the yield stress of the developed supporting fluids. The calculated yield stresses of the fumed silica nanoparticle suspensions at the concentrations of 5, 6, and 7% (w/v) are 34.41, 86.73 and 105.72 Pa, respectively. The mineral oil/6%(w/v) fumed silica supporting fluid with a yield stress of 86.73 Pa shows a good supporting behavior.

Table 1 Parameters of the Herschel-Bulkley fits for the mineral oil/fumed silica supporting fluids with different fumed silica concentrations (data from Fig. 2c).

Fluid type	Yield stress, τ_0 (Pa)	Flow index, n	Consistency index, k (Pa·s^n)
5% (w/v)	34.41 $\pm$ 1.420	0.48 $\pm$ 0.016	7.67 $\pm$ 0.243
6% (w/v)	86.73 $\pm$ 2.410	0.39 $\pm$ 0.006	26.06 $\pm$ 1.041
7% (w/v)	105.72 $\pm$ 1.626	0.37 $\pm$ 0.002	36.56 $\pm$ 1.546

Results are mean $\pm$ 95% confidence interval obtained from three replicates.
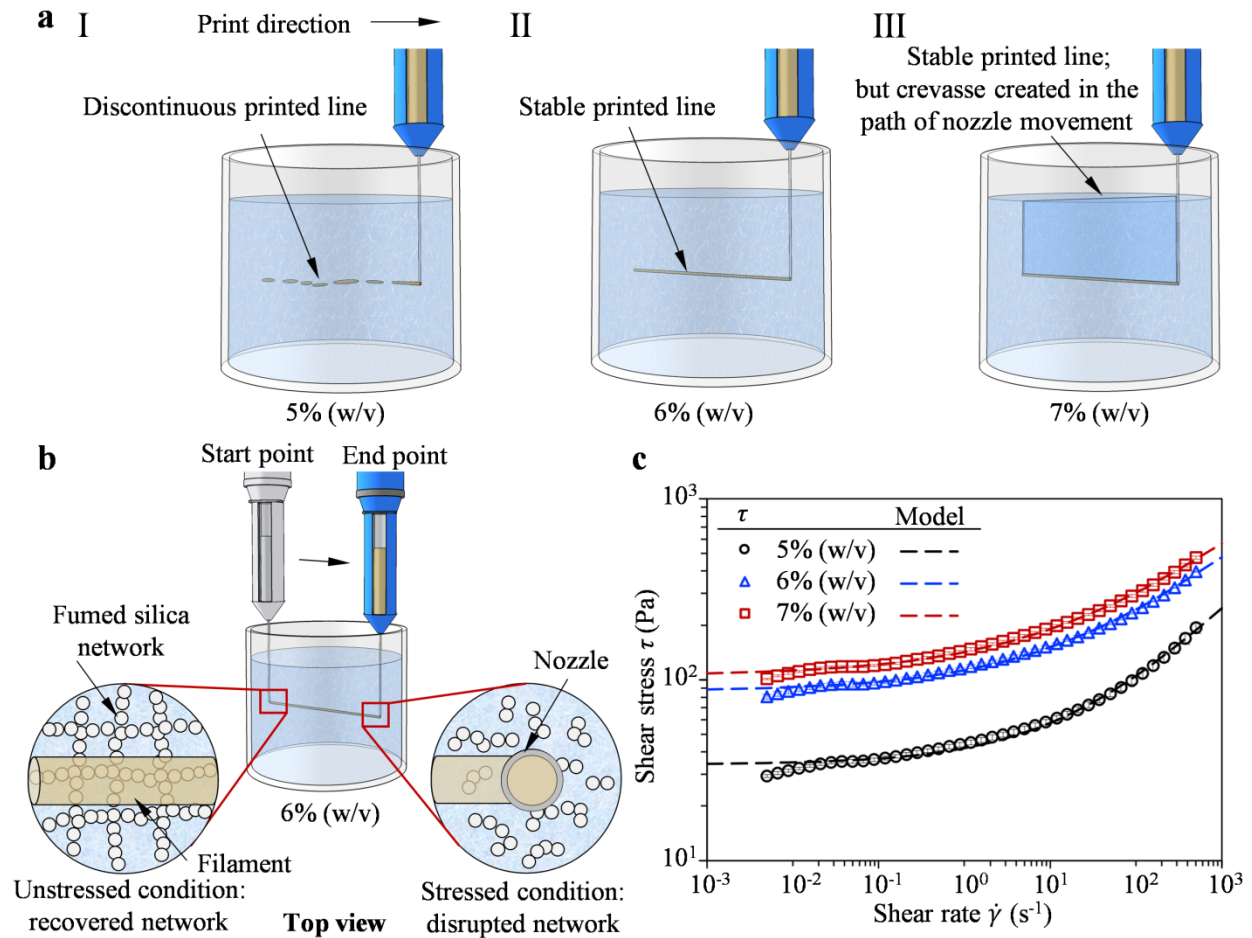
Fig. 2. Characterization of the supporting fluid with different fumed silica concentrations: (a) Schematic of the supporting behavior of the supporting fluids with different fumed silica concentrations (5, 6 and 7% (w/v)). (b) The mechanism of the fumed silica supporting network in unstressed and stressed conditions during the printing process. (c) Shear stress with respect to shear rate of the supporting fluids with different fumed silica concentrations (dashed lines are fitted Herschel-Bulkley models).

Upon the supporting behavior test and the yield stress characterization of the supporting fluid with different fumed silica concentrations, we chose to use mineral oil/6%(w/v) fumed silica supporting fluid in this work. The next step is to find out the piezoelectric and conductive ink compositions. Fig. 3a shows the piezoelectric behavior of the PDMS/PZT composites with different PZT volume fractions: 10, 20, 30 and 40 vol%. Although the PDMS/40vol%PZT composite exhibits the highest d_{33} value of 6.30 pC/N, it usually blocks the nozzle (diameter = 0.6 mm). Thus, we decided to use

13

the PDMS/30vol%PZT composite having a d_{33} value of 4.43 pC/N and exhibiting stable flow through the nozzle as the piezoelectric ink formulation. Fig. 3b depicts the conductive behavior of the PDMS/Ag composites with different Ag volume fractions: 20, 25 and 30 vol%. The PDMS/20vol%Ag composite is not conductive as marked in red. The PDMS/30vol%Ag composite shows the highest conductivity of 17.6 S/m. However, we chose to use the PDMS/25vol%Ag composite because of the high price of Ag nanoflakes.

Fig. 3c-d reports the effect of shear rates on the viscoelastic properties of the PDMS/PZT and PDMS/Ag with different compositions using data from rotational rheometer (at low shear rates) and capillary flow test (at high shear rates). The open symbols in Fig. 3c-d present the viscosity of the composites with different filler concentrations obtained through rotational rheometry with respect to the shear rate. The process-related apparent viscosities of the composites with different filler concentrations are presented by solid symbols in Fig. 3c-d. All inks exhibit a pronounced shear-thinning response as evidenced by an important decrease in viscosity as the share rate increases. For example, the apparent viscosity of the PDMS/30vol%PZT piezoelectric composite ink at a shear rate of around 28 s^{-1} is ~204 Pa·s and nearly 4 orders of magnitude smaller than the viscosity of ~1.8 $\times$ 10^6 Pa·s measured by rotational rheometer at low shear rates. The viscosity of the inks increases with filler content at all shear rates, which will affect 3D printability. The data points gap observed in the shear rate range of $10^0 \leq \dot{\gamma} \leq 10^1$ s^{-1} is due to measurement instabilities in the rotational rheometer caused by material yielding and separating from the parallel plates. Neither was it possible with the capillary flow method, because higher extrusion pressure for the material to flow through the nozzle is required. A power-law (Ostwald de Waele) model is commonly used to assume the shear-thinning behaviour of composite materials [59–61]. The power-law model relates shear viscosity η to shear rate $\dot{\gamma}$ as:

$$\eta = k\dot{\gamma}^{n-1} \qquad (2)$$

where n is the flow index ($0 < n < 1$), and k is the consistency index (Pa·s^n). The respective fitted power-law parameters n and k for each ink formulation are listed in Table 2. Flow index values $n < 1$ depict the shear-thinning nature of the inks. The model shows good agreement with the rheometry and capillary data in both low and high $\dot{\gamma}$ regions, confirming the choice of the power-law viscosity model to describe the shear-thinning behavior of the developed inks.

Table 2 Parameters of the power-law fits for the piezoelectric and conductive composite inks with different filler contents (data from Fig. 3c-d).

Ink type	Flow index, n	Consistency index, k (Pa·s^n)
PDMS/10vol%PZT	0.274 ± 0.0082	128 ± 0.9
PDMS/20vol%PZT	0.201 ± 0.0091	530 ± 0.8
PDMS/30vol%PZT	0.159 ± 0.0103	3,692 ± 1.6
PDMS/25vol%Ag	0.268 ± 0.0176	3,986 ± 1.2
PDMS/30vol%Ag	0.248 ± 0.0102	10,206 ± 6.8

Results are mean ± 95% confidence interval obtained from three replicates.

Mechanical tensile tests were carried out to investigate the mechanical behavior (i.e., mechanical stretchability) of the selected formulations i.e., the PDMS/30vol%PZT piezoelectric composite and PDMS/25vol%Ag conductive composite compositions as they show the highest piezoelectric or conductive properties while being printable (shear-thinning behavior, $n < 1$). Fig. 3e-f show the average stress-strain curves of the three tested replicates. All types of piezoelectric and conductive composite films show a relatively long linear regime. The ultimate stress at failure and stiffness are improving with filler concentration. We found that both the PDMS/30vol%PZT piezoelectric composite (ultimate stress at failure = 2.86 ± 0.067 MPa; Young's modulus = 9.7 ± 0.020 MPa) and PDMS/25vol%Ag conductive composite (ultimate stress at failure = 1.59 ±

15

0.076 MPa; Young's modulus = 8.2 $\pm$ 0.046 MPa) exhibit an elongation at break of up to 30%, making them well suited for flexible or soft piezoelectric sensing devices.
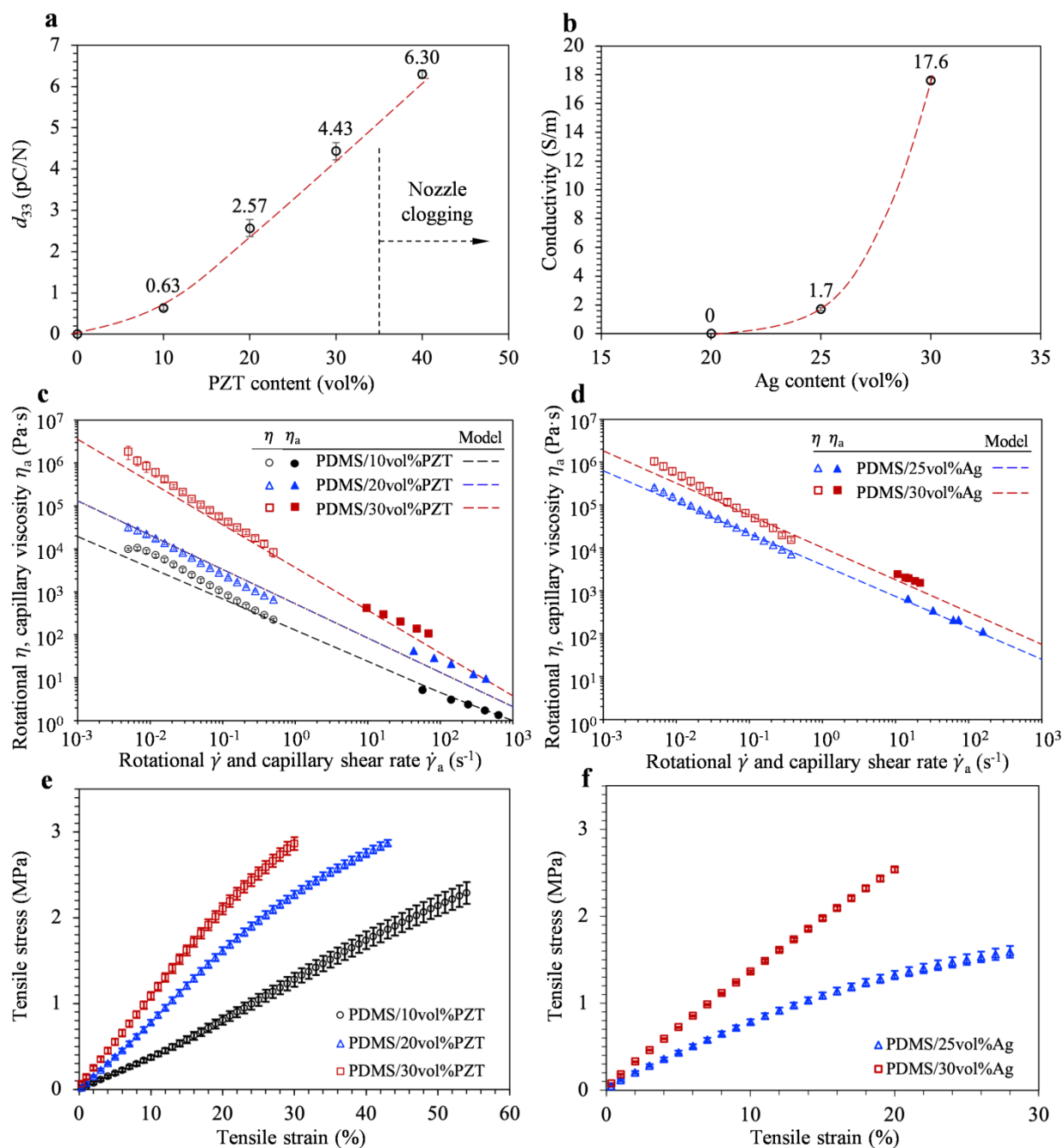

Fig. 3. Characterization of the developed flexible piezoelectric PDMS/PZT and conductive PDMS/Ag composite materials: (a) d_{33} of piezoelectric composites with different PZT volume fractions. (b) Conductivity of conductive composites with different Ag volume fractions (dashed lines are trend lines). (c-d) Viscoelastic (dashed lines are fitted shear-thinning power-law models), and (e-f) mechanical properties of the piezoelectric and conductive composites with different filler

16

concentrations. Error bars indicate 95% confidence interval of the mean obtained from three replicates.

Three types of piezoelectric composite structures as demonstrators were designed and fabricated: a multi-layer planar film, a conformal non-planar hemisphere and a freeform spiral-hexagon (Fig. 4a). The dimensions of the fabricated structures are listed in Table S1. The maximum geometrical error compared to the designed model is ~3.5%, which indicates that the dimensional accuracy of this printing technique is acceptable. The images of the printed structures within or out of the supporting bath indicate that the patterned features do retain their shape after the printing and curing processes (Fig. 4b-c).
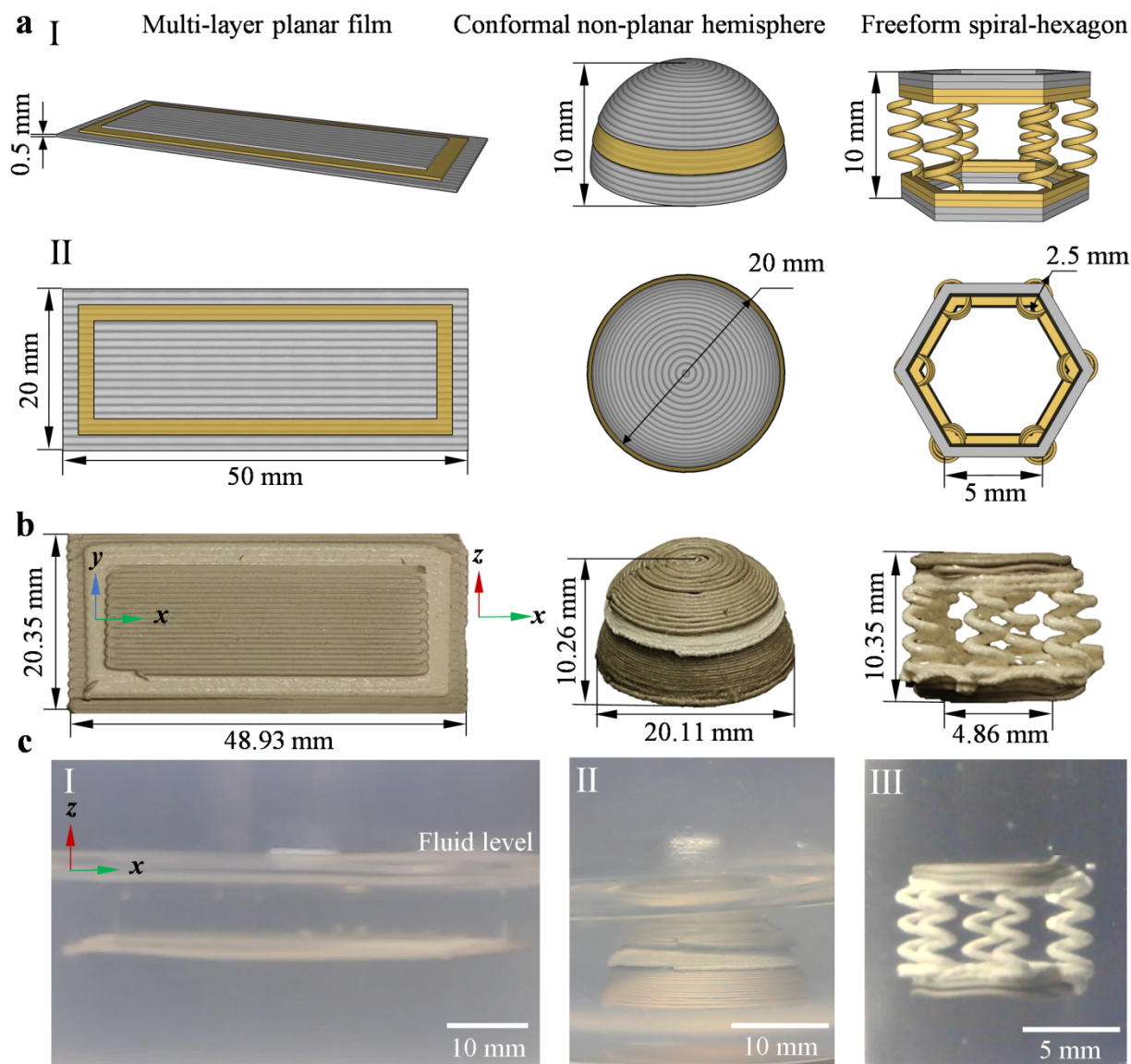
Fig. 4. Design of the multi-material 3D printed flexible piezoelectric composite sensors with integrated electrodes: (a) 3D models (I: front view; II: top view), (b) Images of the cured structures taken out of the supporting fluid, and (c) Images of the uncured structures in the supporting fluid after the printing process of the three types of multi-material 3D printed flexible piezoelectric composite structures with integrated electrodes: a multi-layer planar film, a conformal non-planar hemisphere and a freeform spiral-hexagon.

Fig. 5a shows the locations of the samples cut from the three types of multi-material 3D printed piezoelectric composite sensors with integrated electrodes for SEM observations. We observed that the SEM images in Fig. 5b show no significant oil trapped between the electrode and

18

piezoelectric layers, demonstrating the good bonding between the layers of the multi-material 3D printed piezoelectric sensors. Fig. 5cI-dI show the SEM images taken from the piezoelectric and conductive layers of the conformal non-planar hemisphere. The printed filaments are uniform (width = ~0.495 mm) and no significant porosities between filaments is observed. Fig. 5cII-dII show the transverse cross-section view and Fig. 5cIII-dIII show the enlarged view of the deposited filaments. For both composites, the PZT or Ag fillers are well-dispersed in the PDMS matrix without any significant agglomerations. Fig. 5e shows the piezoelectric composite spiral cut from the freeform spiral-hexagon. We observed that the diameter of the spiral is uniform (~2.58 mm) and the pitches (~1.91 mm) between the turns are identical.
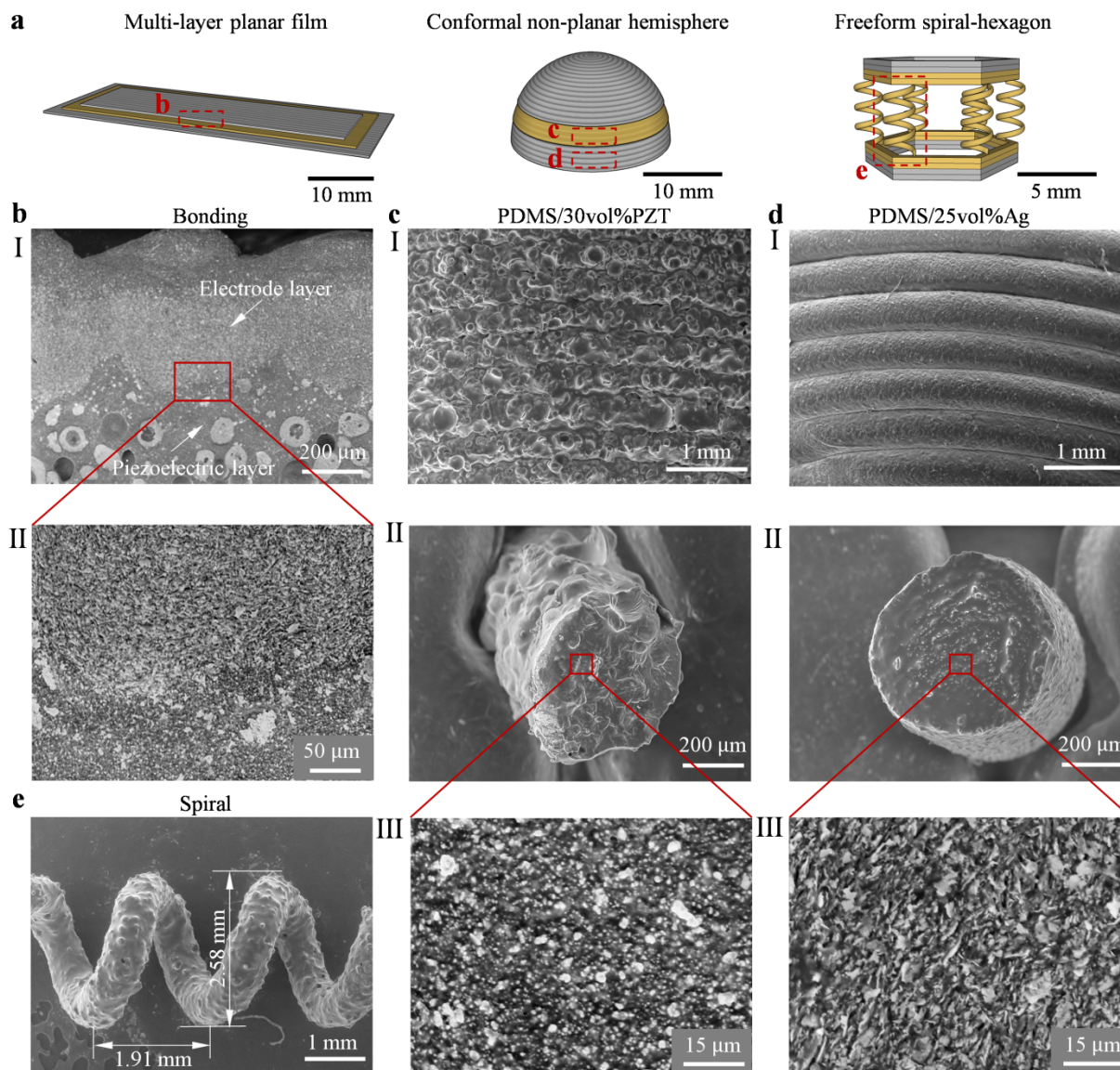
Fig. 5. SEM images of the multi-material 3D printed flexible piezoelectric composite sensors with integrated electrodes: (a) The locations of the samples cut from the three types of piezoelectric sensors. (b) SEM images of the bonding between the conductive and piezoelectric layers of the multi-layer planar film (II: enlarged view). (c) PDMS/30vol%PZT piezoelectric composite: (I) surface view of the sample cut from the piezoelectric layer of the conformal non-planar hemisphere, (II) transverse cross-section view of the deposited filaments (III: enlarged view). (d) PDMS/25vol%Ag conductive composite: (I) surface view of the sample cut from the conductive layer of the conformal non-planar hemisphere, (II) transverse cross-section view of the deposited filaments (III: enlarged view). (e) A PDMS/30vol%PZT composite spiral cut from the freeform spiral-hexagon.

20

As listed in Table 3, we conducted the stretching or compression tests to evaluate the piezoelectric performance of the three demonstrators. The piezoelectric performance as a function of cyclic axial elongation was investigated by extending the multi-layer planar film to 10% strain at a crosshead speed of 1 mm/s and relaxing it back to a zero-strain condition at the same rate. This stretching-relaxation cycle was repeated three times. The obtained peak-to-peak voltage (V_{pp}) is 41.14 $\pm$ 0.316 mV (Fig. 6a). The piezoelectric signal is consistent with the applied strain with negligible variation. For the conformal non-planar hemisphere (Fig. 6b), we pressed it with a finger three times. The V_{pp} is 152.43 $\pm$ 4.624 mV. We observed that during the press-release cycle, the upper part of the hemisphere is dented inside but it will bounce out automatically, which shows its great potential to be used as a battery-free flexible button. To validate the durability of the freeform spiral-hexagon, we compressed it with a displacement of 2 mm at 8 Hz for 800 cycles using a shaker (Fig. 6c). The V_{pp} of the early cycles is 88.53 $\pm$ 1.224 mV and the V_{pp} of the late cycles is 86.39 $\pm$ 1.145 mV, which indicates that the freeform spiral-hexagon still shows favorable stability for more than 800 cycles without much degradation.

Table 3 Comparison of the developed three demonstrators.

Type	Multi-layer planar film	Conformal non-planar hemisphere	Freeform spiral-hexagon
Mode	Tension	Bending	Compression and shearing
V_{pp} (mV)	41.14 $\pm$ 0.316 Strain = 10%	152.43 $\pm$ 4.624 Under three finger taps	86.39 $\pm$ 1.145 Displacement = 2 mm 8 Hz for 800 cycles
Weight (g)	3.52 $\pm$ 0.079	3.69 $\pm$ 0.069	0.45 $\pm$ 0.060
Advantages	• Extensible	• More flexible • Spring back behavior • More compact than planar design	• More complex shape • Spring back behavior • Freedom in design • Easily tailor the stiffness

Results are mean $\pm$ 95% confidence interval obtained from three replicates.
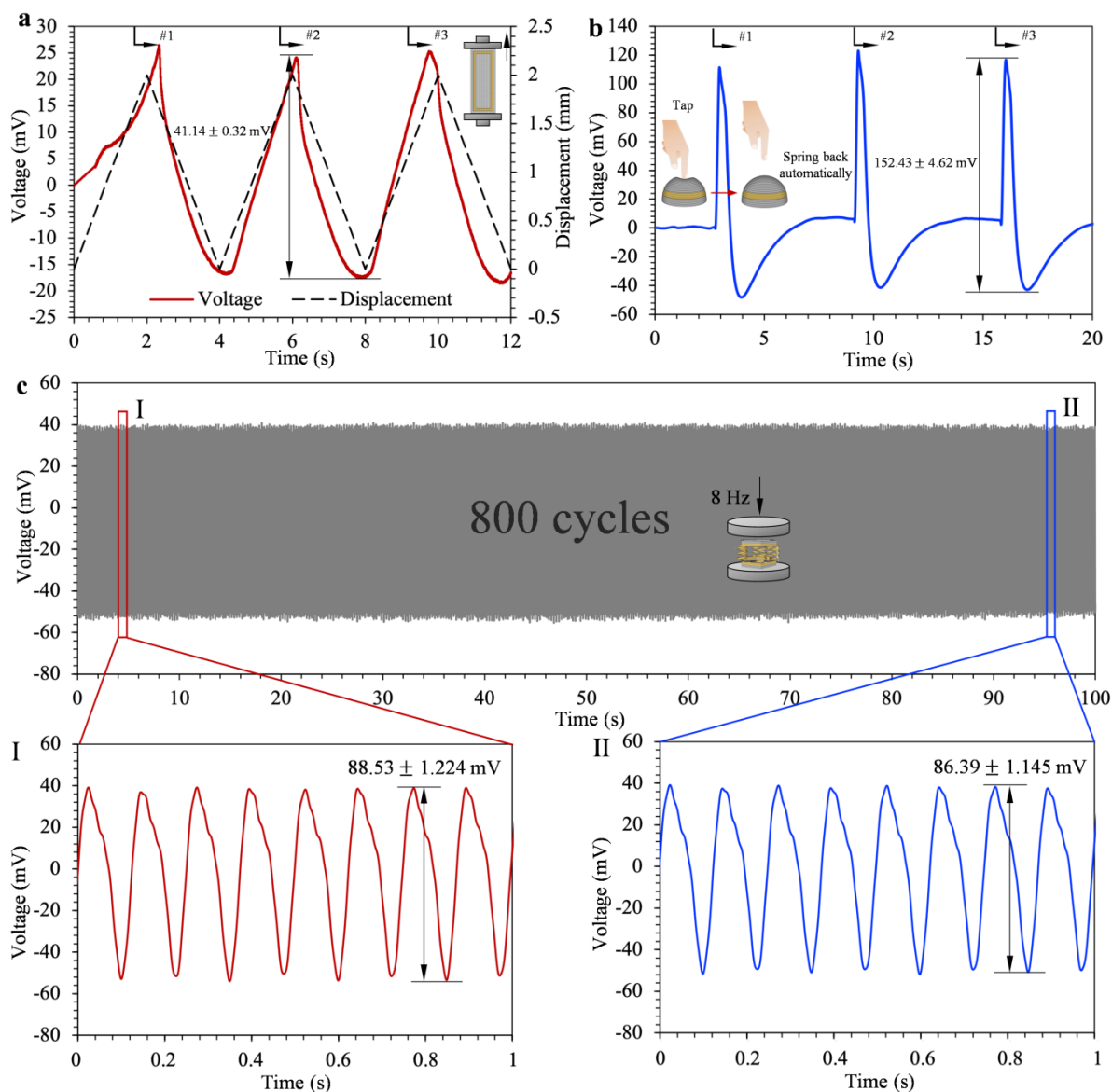
Fig. 6. Piezoelectric characterizations of the multi-material 3D printed flexible piezoelectric composite sensors with integrated electrodes: (a) Stretching-relaxation test on the multi-layer planar film (50 × 20 × 1.5 mm^3) with a strain up to 10% for 3 cycles. (b) Finger tapping test on the conformal non-planar hemisphere for 3 cycles. (c) Cyclic compression test on the freeform spiral-hexagon with a displacement of 2 mm at 8 Hz for 800 cycles (Inset figures I: for the early 8 cycles; II: for the late 8 cycles.).

4. Conclusion

22

We have successfully implemented a multi-material DIW layer-by-layer, conformal (non-planar) and freeform 3D printing technique to fabricate flexible piezoelectric composite sensors with integrated electrodes inside a supporting fluid. The characterization on the tailored piezoelectric PDMS/30vol%PZT and conductive PDMS/25vol%Ag composite inks show that the inks meet the functional requirements to be used as the piezoelectric sensing element and the electrodes while being 3D printable (e.g., shear-thinning behavior) and mechanically flexible (up to 30% elongation at break for both composites). The mineral oil/6%(w/v) fumed silica nanoparticle suspension with the proper yield stress is found to successfully facilitate freeform 3D printing of the developed piezoelectric and conductive inks. For demonstration, three types of multi-material 3D printed piezoelectric composite structures are fabricated and tested to assess their piezoelectric performance. For example, under cyclic compression test at 8 Hz, the V_{pp} of a freeform spiral-hexagon is 86.39 ± 1.145 mV for more than 800 cycles. The novel approach presented here provides new opportunities to fabricate flexible piezoelectric devices with integrated electrodes in other complex freeform geometries, using a clean (i.e., without the need of toxic solvents) and eco-friendly (i.e., the supporting fluid is reusable) fabrication process, with high shape fidelity, easy operational mode (i.e., multi-material DIW 3D printing in a single manufacturing process) for piezoelectric sensing or energy harvesting devices in biomedical fields.

Acknowledgement

for the advice on the analysis of rheological properties, Dr. Mohammad Rafiee and Mr. Abraham Bhérer-Constant for the training on Aerotech gantry system.

Declaration of competing interest

No author associated with this paper has disclosed any potential or pertinent conflicts which may be perceived to have impending conflict with this work.

Electronic copy available at: https://ssrn.com/abstract=4110389

References

[1]   Z. Wang, X. Yuan, J. Yang, Y. Huan, X. Gao, Z. Li, H. Wang, S. Dong, 3D-printed flexible, Ag-coated PNN-PZT ceramic-polymer grid-composite for electromechanical energy conversion, Nano Energy. 73 (2020) 104737. https://doi.org/10.1016/j.nanoen.2020.104737.

[2]   A. Rovisco, A. Dos Santos, T. Cramer, J. Martins, R. Branquinho, H. Águas, B. Fraboni, E. Fortunato, R. Martins, R. Igreja, P. Barquinha, Piezoelectricity Enhancement of Nanogenerators Based on PDMS and ZnSnO3Nanowires through Microstructuration, ACS Appl. Mater. Interfaces. 12 (2020) 18421–18430. https://doi.org/10.1021/acsami.9b21636.

[3]   Q. Zheng, H. Zhang, H. Mi, Z. Cai, Z. Ma, S. Gong, High-performance flexible piezoelectric nanogenerators consisting of porous cellulose nanofibril (CNF)/poly(dimethylsiloxane) (PDMS) aerogel films, Nano Energy. 26 (2016) 504–512. https://doi.org/10.1016/j.nanoen.2016.06.009.

[4]   K. Shi, X. Huang, B. Sun, Z. Wu, J. He, P. Jiang, Cellulose/BaTiO 3 aerogel paper based flexible piezoelectric nanogenerators and the electric coupling with triboelectricity, Nano Energy. 57 (2019) 450–458. https://doi.org/10.1016/j.nanoen.2018.12.076.

[5]   X. Ren, H. Fan, Y. Zhao, Z. Liu, Flexible Lead-Free BiFeO3/PDMS-Based Nanogenerator as Piezoelectric Energy Harvester, ACS Appl. Mater. Interfaces. 8 (2016) 26190–26197. https://doi.org/10.1021/acsami.6b04497.

[6]   J.E.Q. Quinsaat, T. de Wild, F.A. Nüesch, D. Damjanovic, R. Krämer, G. Schürch, D. Häfliger, F. Clemens, T. Sebastian, M. Dascalu, D.M. Opris, Stretchable piezoelectric elastic composites for sensors and energy generators, Compos. Part B Eng. 198 (2020). https://doi.org/10.1016/j.compositesb.2020.108211.

[7]   C. Luo, S. Hu, M. Xia, P. Li, J. Hu, G. Li, H. Jiang, W. Zhang, A Flexible Lead-Free BaTiO3/PDMS/C Composite Nanogenerator as a Piezoelectric Energy Harvester, Energy Technol. 6 (2018) 922–927. https://doi.org/10.1002/ente.201700756.

[8]   H. Cui, R. Hensleigh, D. Yao, D. Maurya, P. Kumar, M.G. Kang, S. Priya, X. Zheng, Three-dimensional printing of piezoelectric materials with designed anisotropy and directional response, Nat. Mater. 18 (2019) 234–241. https://doi.org/10.1038/s41563-018-0268-1.

[9]   D. Yao, H. Cui, R. Hensleigh, P. Smith, S. Alford, D. Bernero, S. Bush, K. Mann, H.F. Wu, M. Chin-Nieh, G. Youmans, X. Zheng, Achieving the Upper Bound of Piezoelectric Response in Tunable, Wearable 3D Printed Nanocomposites, Adv. Funct. Mater. 29 (2019). https://doi.org/10.1002/adfm.201903866.

[10]   S. Chen, W.S. Tan, M.A. Bin Juhari, Q. Shi, X.S. Cheng, W.L. Chan, J. Song, Freeform 3D printing of soft matters: recent advances in technology for biomedical engineering, Biomed. Eng. Lett. 10 (2020) 453–479. https://doi.org/10.1007/s13534-020-00171-8.

[11]   R.D. Farahani, K. Chizari, D. Therriault, Three-dimensional printing of freeform helical microstructures: A review, Nanoscale. 6 (2014) 10470–10485. https://doi.org/10.1039/c4nr02041c.

[12]   N. Bausch, D.P. Dawkins, R. Frei, Inspired - Advances in Conformal Printing: 3D Printing onto Unknown Uneven Surfaces, IEEE/ASME Int. Conf. Adv. Intell. Mechatronics, AIM. (2017) 430–435. https://doi.org/10.1109/AIM.2017.8014055.

[13]   S.G. Patrício, L.R. Sousa, T.R. Correia, V.M. Gaspar, L.S. Pires, J.L. Luís, J.M. Oliveira, J.F. Mano, Freeform 3D printing using a continuous viscoelastic supporting matrix, Biofabrication. 12 (2020). https://doi.org/10.1088/1758-5090/ab8bc3.

[14] R.A. Barry, R.F. Shepherd, J.N. Hanson, R.G. Nuzzo, P. Wiltzius, J.A. Lewis, Direct-write assembly of 3D hydrogel scaffolds for guided cell growth, Adv. Mater. 21 (2009) 2407–2410. https://doi.org/10.1002/adma.200803702.

[15] Q. Wu, D. Therriault, M.C. Heuzey, Processing and Properties of Chitosan Inks for 3D Printing of Hydrogel Microstructures, ACS Biomater. Sci. Eng. 4 (2018) 2643–2652. https://doi.org/10.1021/acsbiomaterials.8b00415.

[16] H. Wei, X. Cauchy, I.O. Navas, Y. Abderrafai, K. Chizari, U. Sundararaj, Y. Liu, J. Leng, D. Therriault, Direct 3D Printing of Hybrid Nanofiber-Based Nanocomposites for Highly Conductive and Shape Memory Applications, ACS Appl. Mater. Interfaces. 11 (2019) 24523–24532. https://doi.org/10.1021/acsami.9b04245.

[17] R.D. Farahani, H. Dalir, V. Le Borgne, L.A. Gautier, M.A. El Khakani, M. Lévesque, D. Therriault, Direct-write fabrication of freestanding nanocomposite strain sensors, Nanotechnology. 23 (2012). https://doi.org/10.1088/0957-4484/23/8/085502.

[18] L.L. Lebel, B. Aissa, M.A. El Khakani, D. Therriault, Ultraviolet-assisted direct-write fabrication of carbon nanotube/polymer nanocomposite microcoils, Adv. Mater. 22 (2010) 592–596. https://doi.org/10.1002/adma.200902192.

[19] B. Herren, M.C. Saha, M.C. Altan, Y. Liu, Development of ultrastretchable and skin attachable nanocomposites for human motion monitoring via embedded 3D printing, Compos. Part B Eng. 200 (2020) 108224. https://doi.org/10.1016/j.compositesb.2020.108224.

[20] F. Li, P. Smejkal, N.P. Macdonald, R.M. Guijt, M.C. Breadmore, One-Step Fabrication of a Microfluidic Device with an Integrated Membrane and Embedded Reagents by Multimaterial 3D Printing, Anal. Chem. 89 (2017) 4701–4707. https://doi.org/10.1021/acs.analchem.7b00409.

[21] A.K. Grosskopf, R.L. Truby, H. Kim, A. Perazzo, J.A. Lewis, H.A. Stone, Viscoplastic Matrix Materials for Embedded 3D Printing, ACS Appl. Mater. Interfaces. 10 (2018) 23353–23361. https://doi.org/10.1021/acsami.7b19818.

[22] R.L. Truby, M. Wehner, A.K. Grosskopf, D.M. Vogt, S.G.M. Uzel, R.J. Wood, J.A. Lewis, Soft Somatosensitive Actuators via Embedded 3D Printing, Adv. Mater. 30 (2018) 1–8. https://doi.org/10.1002/adma.201706383.

[23] J. Zhao, M. Hussain, M. Wang, Z. Li, N. He, Embedded 3D printing of multi-internal surfaces of hydrogels, Addit. Manuf. 32 (2020) 101097. https://doi.org/10.1016/j.addma.2020.101097.

[24] W. Hua, K. Mitchell, L. Raymond, B. Godina, D. Zhao, W. Zhou, Y. Jin, Fluid Bath-Assisted 3D Printing for Biomedical Applications: From Pre: From Postprinting Stages, ACS Biomater. Sci. Eng. 7 (2021) 4736–4756. https://doi.org/10.1021/acsbiomaterials.1c00910.

[25] C.S. O'Bryan, T. Bhattacharjee, S. Hart, C.P. Kabb, K.D. Schulze, I. Chilakala, B.S. Sumerlin, W.G. Sawyer, T.E. Angelini, Self-assembled micro-organogels for 3D printing silicone structures, Sci. Adv. 3 (2017). https://doi.org/10.1126/sciadv.1602800.

[26] C. Pellet, M. Cloitre, The glass and jamming transitions of soft polyelectrolyte microgel suspensions, Soft Matter. 12 (2016) 3710–3720. https://doi.org/10.1039/c5sm03001c.

[27] Y. Jin, K. Song, N. Gellermann, Y. Huang, Printing of hydrophobic materials in fumed silica nanoparticle suspension, ACS Appl. Mater. Interfaces. (2019). https://doi.org/10.1021/acsami.9b07433.

[28] Y. Jin, A. Compaan, W. Chai, Y. Huang, Functional Nanoclay Suspension for Printing-

26

Then-Solidification of Liquid Materials, ACS Appl. Mater. Interfaces. 9 (2017) 20057–20066. https://doi.org/10.1021/acsami.7b02398.

[29] Y. Jin, R. Xiong, P.J. Antonelli, C.J. Long, C.W. McAleer, J.J. Hickman, Y. Huang, Nanoclay Suspension-Enabled Extrusion Bioprinting of Three-Dimensional Soft Structures, J. Manuf. Sci. Eng. 143 (2021) 1–9. https://doi.org/10.1115/1.4051010.

[30] R. Karyappa, M. Hashimoto, Freeform Polymer Precipitation in Microparticulate Gels, ACS Appl. Polym. Mater. 3 (2021) 908–919. https://doi.org/10.1021/acsapm.0c01208.

[31] T. Bhattacharjee, S.M. Zehnder, K.G. Rowe, S. Jain, R.M. Nixon, W.G. Sawyer, T.E. Angelini, Writing in the granular gel medium, Sci. Adv. 1 (2015) 1–7. https://doi.org/10.1126/sciadv.1500655.

[32] S. Abdollahi, E.J. Markvicka, C. Majidi, A.W. Feinberg, 3D Printing Silicone Elastomer for Patient-Specific Wearable Pulse Oximeter, Adv. Healthc. Mater. 9 (2020). https://doi.org/10.1002/adhm.201901735.

[33] Y. Jin, A. Compaan, T. Bhattacharjee, Y. Huang, Granular gel support-enabled extrusion of three-dimensional alginate and cellular structures, Biofabrication. 8 (2016). https://doi.org/10.1088/1758-5090/8/2/025016.

[34] S. Yang, H. Tang, C. Feng, J. Shi, J. Yang, The research on multi-material 3D vascularized network integrated printing technology, Micromachines. 11 (2020) 1–13. https://doi.org/10.3390/mi11030237.

[35] A. Basu, A. Saha, C. Goodman, R.T. Shafranek, A. Nelson, Catalytically Initiated Gel-in-Gel Printing of Composite Hydrogels, ACS Appl. Mater. Interfaces. 9 (2017) 40898–40904. https://doi.org/10.1021/acsami.7b14177.

[36] G. Cidonio, M. Cooke, M. Glinka, J.I. Dawson, L. Grover, R.O.C. Oreffo, Printing bone in a gel: using nanocomposite bioink to print functionalised bone scaffolds, Mater. Today Bio. 4 (2019) 100028. https://doi.org/10.1016/j.mtbio.2019.100028.

[37] A.M. Compaan, K. Song, Y. Huang, Gellan Fluid Gel as a Versatile Support Bath Material for Fluid Extrusion Bioprinting, ACS Appl. Mater. Interfaces. (2019). https://doi.org/10.1021/acsami.8b13792.

[38] E. Mirdamadi, J.W. Tashman, D.J. Shiwarski, R.N. Palchesko, A.W. Feinberg, FRESH 3D Bioprinting a Full-Size Model of the Human Heart, ACS Biomater. Sci. Eng. 6 (2020) 6453–6459. https://doi.org/10.1021/acsbiomaterials.0c01133.

[39] O. Jeon, Y. Bin Lee, H. Jeong, S.J. Lee, D. Wells, E. Alsberg, Individual cell-only bioink and photocurable supporting medium for 3D printing and generation of engineered tissues with complex geometries, Mater. Horizons. 6 (2019) 1625–1631. https://doi.org/10.1039/c9mh00375d.

[40] T.J. Hinton, A. Hudson, K. Pusch, A. Lee, A.W. Feinberg, 3D Printing PDMS Elastomer in a Hydrophilic Support Bath via Freeform Reversible Embedding, ACS Biomater. Sci. Eng. 2 (2016) 1781–1786. https://doi.org/10.1021/acsbiomaterials.6b00170.

[41] F. Afghah, M. Altunbek, C. Dikyol, B. Koc, Preparation and characterization of nanoclay-hydrogel composite support-bath for bioprinting of complex structures, Sci. Rep. 10 (2020) 1–13. https://doi.org/10.1038/s41598-020-61606-x.

[42] A. Colly, C. Marquette, E.J. Courtial, Poloxamer/Poly(ethylene glycol) Self-Healing Hydrogel for High-Precision Freeform Reversible Embedding of Suspended Hydrogel, Langmuir. 37 (2021) 4154–4162. https://doi.org/10.1021/acs.langmuir.1c00018.

[43] E.L. Tang, L. Wang, Y.F. Han, Space debris positioning based on two-dimensional PVDF piezoelectric film sensor, Adv. Sp. Res. 63 (2019) 2410–2421.

https://doi.org/10.1016/j.asr.2018.12.035.

[44] P. Zhu, Y. Wang, Y. Wang, H. Mao, Q. Zhang, Y. Deng, Flexible 3D Architectured Piezo/Thermoelectric Bimodal Tactile Sensor Array for E-Skin Application, Adv. Energy Mater. 10 (2020) 1–8. https://doi.org/10.1002/aenm.202001945.

[45] G. Cho, K. Jeong, M.J. Paik, Y. Kwun, M. Sung, Performance evaluation of textile-based electrodes and motion sensors for smart clothing, IEEE Sens. J. 11 (2011) 3183–3193. https://doi.org/10.1109/JSEN.2011.2167508.

[46] F. Mokhtari, M. Shamshirsaz, M. Latifi, J. Foroughi, Nanofibers-based piezoelectric energy harvester for self-powered wearable technologies, Polymers (Basel). 12 (2020) 1–15. https://doi.org/10.3390/polym12112697.

[47] G. Haghiashtiani, M.A. Greminger, Fabrication, polarization, and characterization of PVDF matrix composites for integrated structural load sensing, (2015). https://doi.org/10.1088/0964-1726/24/4/045038.

[48] X. Lu, H. Qu, M. Skorobogatiy, Piezoelectric microstructured fibers via drawing of multimaterial preforms, Sci. Rep. 7 (2017) 1–12. https://doi.org/10.1038/s41598-017-01738-9.

[49] X. Lu, H. Qu, M. Skorobogatiy, Piezoelectric Micro- and Nanostructured Fibers Fabricated from Thermoplastic Nanocomposites Using a Fiber Drawing Technique: Comparative Study and Potential Applications, ACS Nano. 11 (2017) 2103–2114. https://doi.org/10.1021/acsnano.6b08290.

[50] S. Bodkhe, C. Noonan, F.P. Gosselin, D. Therriault, Coextrusion of Multifunctional Smart Sensors, Adv. Eng. Mater. 20 (2018) 1800206. https://doi.org/10.1002/adem.201800206.

[51] C. Xu, B. Quinn, L.L. Lebel, D. Therriault, G. L'espérance, Multi-Material Direct Ink Writing (DIW) for Complex 3D Metallic Structures with Removable Supports, ACS Appl. Mater. Interfaces. 11 (2019) 8499–8506. https://doi.org/10.1021/acsami.8b19986.

[52] D. Kokkinis, M. Schaffner, A.R. Studart, Multimaterial magnetically assisted 3D printing of composite materials, Nat. Commun. 6 (2015). https://doi.org/10.1038/ncomms9643.

[53] M.A. Skylar-Scott, J. Mueller, C.W. Visser, J.A. Lewis, Voxelated soft matter via multimaterial multinozzle 3D printing, Nature. 575 (2019) 330–335. https://doi.org/10.1038/s41586-019-1736-8.

[54] A. Yan, X. Yuan, Z. Li, J. Yang, K. Ren, S. Dong, 3D-printed flexible, multilayered ceramic-polymer composite grid with integrated structural-self-sensing function, Sensors Actuators A Phys. 332 (2021) 113187. https://doi.org/10.1016/j.sna.2021.113187.

[55] C. Liu, L. Le, M. Zhang, J. Ding, Tunable Large-Scale Compressive Strain Sensor Based on Carbon Nanotube/Polydimethylsiloxane Foam Composites by Additive Manufacturing, Adv. Eng. Mater. 2101337 (2021) 1–9. https://doi.org/10.1002/adem.202101337.

[56] V. Ozbolat, M. Dey, B. Ayan, A. Povilianskas, M.C. Demirel, I.T. Ozbolat, 3D Printing of PDMS Improves Its Mechanical and Cell Adhesion Properties, ACS Biomater. Sci. Eng. 4 (2018) 682–693. https://doi.org/10.1021/acsbiomaterials.7b00646.

[57] J. Bruneaux, D. Therriault, M.C. Heuzey, Micro-extrusion of organic inks for direct-write assembly, J. Micromechanics Microengineering. 18 (2008). https://doi.org/10.1088/0960-1317/18/11/115020.

[58] P.E.D. Augusto, V. Falguera, M. Cristianini, A. Ibarz, Rheological Behavior of Tomato Juice: Steady-State Shear and Time-Dependent Modeling, Food Bioprocess Technol. 5 (2012) 1715–1723. https://doi.org/10.1007/s11947-010-0472-8.

[59] T. Beran, T. Mulholland, F. Henning, N. Rudolph, T.A. Osswald, Nozzle clogging factors

28

during fused filament fabrication of spherical particle filled polymers, Addit. Manuf. 23 (2018) 206–214. https://doi.org/10.1016/j.addma.2018.08.009.

[60] D. Brzeski, I.L. Hia, J.F. Chauvette, R.D. Farahani, N. Piccirelli, A. Ross, D. Therriault, Design of thermoset composites for high-speed additive manufacturing of lightweight sound absorbing micro-scaffolds, Addit. Manuf. 47 (2021) 102245. https://doi.org/10.1016/j.addma.2021.102245.

[61] J.F. Chauvette, D. Brzeski, I.L. Hia, R.D. Farahani, N. Piccirelli, D. Therriault, High-speed multinozzle additive manufacturing and extrusion modeling of large-scale microscaffold networks, Addit. Manuf. 47 (2021) 102294. https://doi.org/10.1016/j.addma.2021.102294.

Appendix A. Supporting information

Section S1. Images of the supporting behavior of the supporting fluid with different fumed silica concentrations.

Fig. S1 shows the images of a single filament printed in the supporting fluid with three different fumed silica concentrations: 5, 6 and 7% (w/v). The printed filament in the 5% (w/v) supporting fluid were dragged along the movement of the dispensing needle. The printed filament was well-supported in the 6% (w/v) supporting fluid. There was crevasse in the 7% (w/v) supporting fluid caused by the movement of the needle.
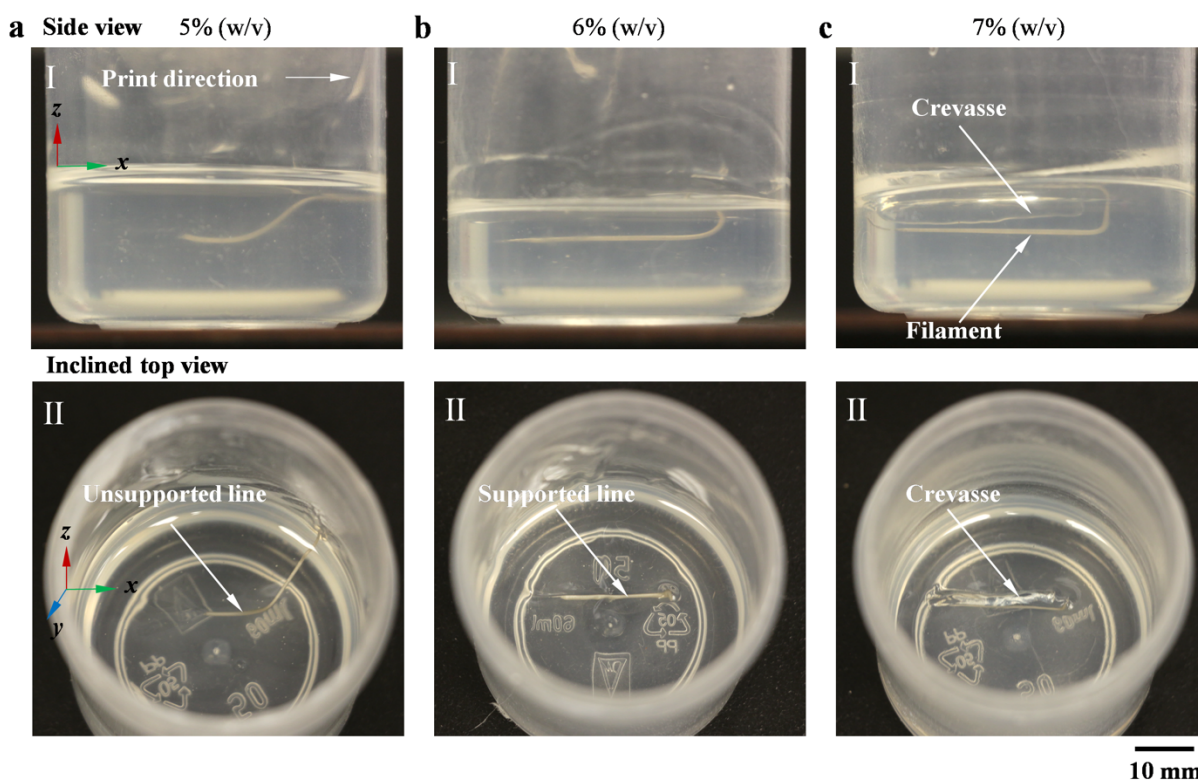

Fig. S1. Images (I: side view and II: inclined top view) of a single PDMS/25vol%Ag conductive composite filament printed in the supporting fluid with different fumed silica concentrations: (a) 5, (b) 6 and (c) 7% (w/v), respectively.

Section S2. Dimension measurement of the three types of piezoelectric composite structures.

Table S1 Dimension measurement of the printed structures (Unit: mm). Error bars indicate 95% confidence interval of the mean obtained from three replicates.

Type		Multi-layer film	Hemisphere	Spiral-hexagon
Length (or diameter or side length)	Measurement	48.93 $\pm$ 0.086	20.26 $\pm$ 0.094	4.86 $\pm$ 0.089
	Model	50	20	5
	Relative error (%)	2.1	1.3	2.8
Width	Measurement	20.35 $\pm$ 0.062	_	_
	Model	20	_	_
	Relative error (%)	1.8	_	_
Height	Measurement	1.55 $\pm$ 0.023	10.11 $\pm$ 0.034	10.35 $\pm$ 0.043
	Model	1.5	10	10
	Relative error (%)	3.3	1.1	3.5

Appendix B. Supplementary movies

Movie S1. Supporting fluid-assisted multi-material 3D printing of a multi-layer planar film piezoelectric sensor.

Movie S2. Supporting fluid-assisted multi-material 3D printing of a conformal non-planar hemisphere piezoelectric sensor.

Movie S3. Supporting fluid-assisted multi-material 3D printing of a freeform spiral-hexagon piezoelectric sensor.